*J Mater Sci* (2019) 54:8426–8435

Electronic materials

# BiOBr nanosheets-decorated $TiO_2$ nanofibers as hierarchical *p–n* heterojunctions photocatalysts for pollutant degradation

Kexin Wang[1], Yongsheng Zhang[1,*], Lina Liu[1], Na Lu[2,*], and Zhenyi Zhang[3]

[1] *Department of Mathematics and Physics, Luoyang Institute of Science and Technology, Luoyang 471023, People's Republic of China*

[2] *Key Laboratory of New Energy and Rare Earth Resource Utilization of State Ethnic Affairs Commission, Key Laboratory of Photosensitive Materials and Devices of Liaoning Province, School of Physics and Materials Engineering, Dalian Nationalities University, 18 Liaohe West Road, Dalian 116600, People's Republic of China*

[3] *School of Materials Science and Engineering, Zhengzhou University, Zhengzhou 450001, People's Republic of China*

**Received:** 9 December 2018
**Accepted:** 18 February 2019
**Published online:** 27 February 2019



## ABSTRACT

Engineering semiconductor-based homo- (hetero-) junctions in hierarchical nanostructures is a promising way to achieve the high performance and recyclable photocatalysts toward pollutants degradation in water. Herein, we develop a kind of hierarchical *p–n* heterojunctions photocatalysts through controllable decoration of ultrathin *p*-BiOBr nanosheets onto *n*-$TiO_2$ electrospun nanofibers by using a traditional solvothermal method. Structural characterization results indicate that the BiOBr nanosheets are assembled uniformly onto the $TiO_2$ nanofibers. This well-designed hierarchical *p–n* heterojunctions in the *p*-BiOBr/*n*-$TiO_2$ nanofibers photocatalyst lead to not only the improved generation/separation of photoinduced charges-carriers, but also the increased amount of redox sites. Benefiting to these advantages, the optimal *p*-BiOBr/*n*-$TiO_2$ nanofibers exhibited the apparent rate constant of 0.1 and 0.15 $min^{-1}$ for photocatalytic RhB and MO degradation under UV-light irradiation, which is twice and three times higher than that of mechanically mixtured BiOBr nanosheets and $TiO_2$ nanofibers, respectively. Control experiments demonstrate that both the photoinduced electrons and the oxygen free radicals play the major roles on the enhancement of photocatalytic activity. Moreover, the *p*-BiOBr/*n*-$TiO_2$ nanofibers photocatalysts with the unique nonwoven structure can be easily recycled without secondary pollution, in particular, still maintaining almost the initial photocatalytic activity during the wastewater treatment.

Address correspondence to E-mail: yszhang@lit.edu.cn; luna@dlnu.edu.cn



https://doi.org/10.1007/s10853-019-03466-z

## Introduction

Semiconductor-based photocatalysis has been regarded as an ideal "green strategy" to confront the increasingly global environmental pollution in modern society. The photocatalysts can harvest solar energy and simultaneously generate active charge carriers for implementing the redox process toward pollutant degradation [1–7]. As the most traditional photocatalyst, *n*-type $TiO_2$ has been widely researched because of its low cost, nontoxicity, long-term stability and the suitable energy levels for producing the reactive species toward the degradation of pollutants [8–10]. Unfortunately, the pure $TiO_2$ is hampered by the rapid recombination rate of photoinduced carriers and low transfer speed. In order to solve these problems, researchers have taken a lot of efforts to construct $TiO_2$-based homo- (hetero-) junction photocatalysts for efficiently facilitating the separation of photoinduced electron–hole [11–16]. Particularly, designing *p*–*n* heterojunctions is of enormous significance because of the existence of an internal electric field, which can greatly accelerate the separation of photogeneration electron–hole and ultimately improve the photocatalytic activity [17–19]. Therefore, seeking a rational *p*-type semiconductor with matchable band-gap structure for *n*-type $TiO_2$ has been endowed with great promise in the development of photocatalytic degradation.

Among the widely reported *p*-type photocatalyst, bismuth oxyhalides (BiOX, X = Cl, Br, I) have been studied extensively in recently years due to the indirect optical transition characteristic and unique layer crystal structure in which excitonic effects can effectively enhance the activities for photocatalytic reactions [20–24]. In particular, bismuth oxybromide (*p*-BiOBr) consisted of a layer of $[Bi_2O_2]^{2+}$ and two layers of bromine ions connected by internal static electric fields along [001] orientation have drawn considerable attention due to its excellent photocatalytic properties [25–28]. Furthermore, BiOBr also has a series of advantages of nontoxic, eco-friendly and low cost in the treatment of contaminants in water and environment [29–31]. In addition, the band-gap structure of *p*-BiOBr and *n*-$TiO_2$ is a well-matched couple as previously reported [32–35]. Therefore, *p*-BiOBr/*n*-$TiO_2$ heterojunctions could take the advantage of internal electric field to prolong the lifetime of reactive species and enhance the photocatalytic activities. Nevertheless, most of the reported *p*-BiOBr/*n*-$TiO_2$ heterojunctions photocatalysts are mainly in powder state. The suspended nanoparticles are very difficult to be separated from the contaminated water after photocatalysis, leading to a secondary pollution. Therefore, it is of great interest to design effective and practical *p*-BiOBr/*n*-$TiO_2$ photocatalysts with both high photocatalytic activities as well as favorable recycling capabilities.

To date, one-dimensional (1D) nanofibers obtained through electrospinning technique have aroused great attention in the field of liquid-phase photocatalysis due to the following advantages: (a) the electrospun nanofibers with abundant functional groups will be the optimal templates for fabricating hierarchical heterojunctions nanostructure and then offer more active reaction sites for connecting with pollutant [36, 37]; (b) the ultra-long nanofiber acts as a vectorial transport "tunnel" for photoinduced electron–hole pairs to acquire a high separation efficiency [38]; (c) the unique feature of nonwoven web structure can not only prevent photocatalysts from agglomerating during photocatalytic process, but also be beneficial to separating and recovering photocatalysts from wastewater after pollutants degradation [39]. On the basis of above, combining *p*-BiOBr with electrospun *n*-$TiO_2$ nanofibers to form a hierarchical *p*–*n* heterostructure would be the ideal method to solve the above problems for practical applications.

In this work, we fabricate a kind of hierarchical *p*-BiOBr/*n*-$TiO_2$ heterojunctions nanofibers (NFs) via the electrospinning technique combined with a traditional solvothermal method. By adjusting the concentrations of Bi and Br sources during solvothermal reaction, the coverage density of ultrathin BiOBr nanosheets on $TiO_2$ NFs could be controlled. This well-designed hierarchical heterojunctions of *p*-BiOBr/*n*-$TiO_2$ NFs exhibit enhanced photocatalytic activity for degradation of both RhB and MO. It could be attributed to the synergistic effects of large surface areas, ultra-long 1D nanostructure and hierarchical *p*–*n* heterojunction. Importantly, the *p*-BiOBr/*n*-$TiO_2$ NFs with unique three-dimensional nonwoven structure could not only effectively avoid the agglomeration of photocatalysts and provide more accessible surface areas for pollutant, but also develop a reliable strategy to facilely separate photocatalysts from liquid system and prevent the secondary pollution. Moreover, the recycled

photocatalysts present desirable structural stability and also retain the initial photocatalytic activity.

## Results and discussion

Figure 1 shows the microstructures of the electrospun $TiO_2$ NFs and *p*-BiOBr/*n*-$TiO_2$ NFs. It can be clearly seen that the $TiO_2$ NF has smooth surface without secondary nanostructures (Fig. 1a). $TiO_2$ NFs with a diameter about 500 nm are aligned in random orientations and interweaved to form a nonwoven nanofibrous film, which is very suitable to serve as active template for different catalytic materials depositing. After the solvothermal treatment, the secondary BiOBr nanosheets are uniformly decorated on the surface of $TiO_2$ NFs (Fig. 1b–d), exhibiting rough surface and increased diameter compared to pure electrospun $TiO_2$ NFs. And the obtained *p*-BiOBr/*n*-$TiO_2$ NFs still maintain the nonwoven nanofibrous structure almost without compromising. Moreover, increasing the concentration of Bi source and Br source during the solvothermal reaction, there is an increased density of BiOBr nanosheets growing on the $TiO_2$ NFs along the long axial direction. This leads to that the interspace between BiOBr nanosheets becomes increasingly narrower, and finally, the $TiO_2$ NF is completely covered by BiOBr nanosheets for BiOBr/$TiO_2$-3. It should be noted that the large amount deposition of BiOBr nanosheets not only can increase the accessible surface areas with pollution, but also can provide numerous active sites for redox reactions which may have important influence on photocatalytic activity.

The typical TEM and HRTEM images of individual BiOBr/$TiO_2$-2 are shown in Fig. 1e, f, respectively. In Fig. 1e, it can be further observed that a large number of BiOBr nanosheets are tightly decorated on the surface of $TiO_2$ NFs. This is coinciding with the results of the SEM observation. The HRTEM image displays two types of clear lattice fringes in Fig. 1f. One set of the fringes spacing is ca. 0.352 nm, corresponding to the (1 0 1) plane of the anatase crystal structure of $TiO_2$. Another set of the fringes spacing is ca. 0.278 nm, which corresponds to the (1 1 0) lattice spacing of the tetragonal phase BiOBr.

The XRD patterns of the obtained samples are shown in Fig. 2. The electrospun $TiO_2$ NFs are pure anatase phase (JCPDS 21-1272), and the BiOBr nanosheets prepared are tetragonal BiOBr (JCPDS25-0390). The *p*-BiOBr/*n*-$TiO_2$ NFs possess the feature peaks of both $TiO_2$ NFs and BiOBr nanosheets, indicating that the BiOBr nanosheets have been successfully loaded on electrospun $TiO_2$ NFs through the solvothermal method. Moreover, it should be also noted that the diffraction peaks of $TiO_2$ are weakened with the increasing amount of Bi and Br sources, whereas the peak intensities of BiOBr increase gradually in the composite nanofibers. The sharp diffraction peaks of both BiOBr and $TiO_2$ indicate their good crystallinity. No traces of other phases are detected, further confirming the high purity of these as-fabricated *p*-BiOBr/*n*-$TiO_2$ NFs samples.

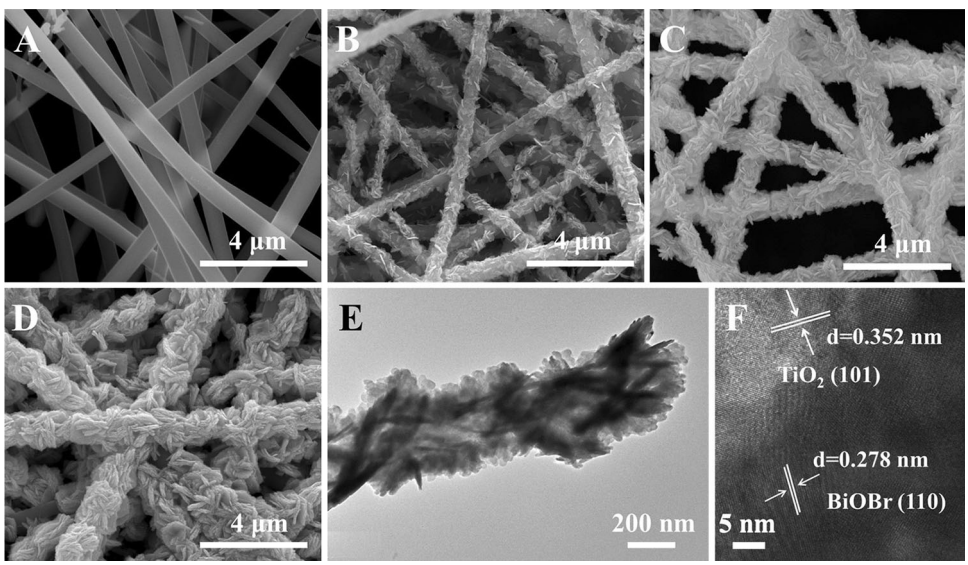


**Figure 1** SEM images of **a** $TiO_2$ NFs; **b** BiOBr/$TiO_2$-1; **c** BiOBr/$TiO_2$-2; **d** BiOBr/$TiO_2$-3. **e** TEM and **f** HRTEM images of BiOBr/$TiO_2$-2.

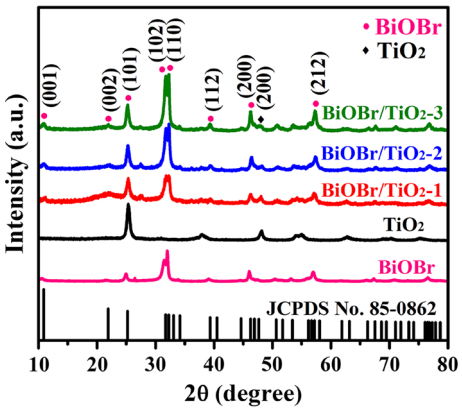


**Figure 2** XRD patterns of BiOBr nanosheets, $TiO_2$ NFs and *p*-BiOBr/*n*-$TiO_2$ NFs.

To further study the surface composition and chemical state of the BiOBr/$TiO_2$-2 sample, XPS analysis was conducted as illustrated in Fig. 3. The typical high-resolution XPS spectrum of Bi 4f region shows a binding energy at 164.5 eV for Bi $4f_{5/2}$ and at 159.2 eV for Bi $4f_{7/2}$, which indicates a normal state of $Bi^{3+}$ in BiOBr/$TiO_2$-2 (Fig. 3a) [40]. The binding energies for Br $3d_{5/2}$ and Br $3d_{7/2}$ are 35.5 eV and 37.6 eV suggesting that the existing Br element is in the chemical state of $Br^-$ (Fig. 3b) [41]. The XPS spectrum for O1 s can be deconvoluted into three peaks at 529.6, 530.5 and 531.9 eV, which can be assigned to Bi–O and Ti–O in BiOBr/$TiO_2$-2 and H–O on surface, respectively (Fig. 3c). The splitting peak between Ti $2p_{1/2}$ and Ti $2p_{3/2}$ in Fig. 3d is 5.7 eV, indicating a normal state of $Ti^{4+}$ in both electrospun $TiO_2$ NFs and the BiOBr/$TiO_2$-2 [42]. This result reveals the coexistence of $TiO_2$ and BiOBr species in the BiOBr/$TiO_2$-2 sample, which is in good accordance with the XRD, TEM and SEM results. Based on the above, the *p*-BiOBr/*n*-$TiO_2$ with rational design *p*–*n* heterostructure has been fabricated successfully, in particular, which will broaden the absorbed light spectrum range as well as facilitate the charge separation rate between BiOBr and $TiO_2$ for efficient degradation of pollutant substance.

The optical properties of $TiO_2$, BiOBr/$TiO_2$-1, BiOBr/$TiO_2$-2, BiOBr/$TiO_2$-3 and BiOBr were examined using the UV–Vis diffuse reflectance spectrum. Figure 4a shows the UV–Vis absorption spectra converted from corresponding diffuse reflectance spectra by means of the Kubelka–Munk function [43]:

$$F(R) = (1-R)^2/2R = \alpha/S \quad (1)$$

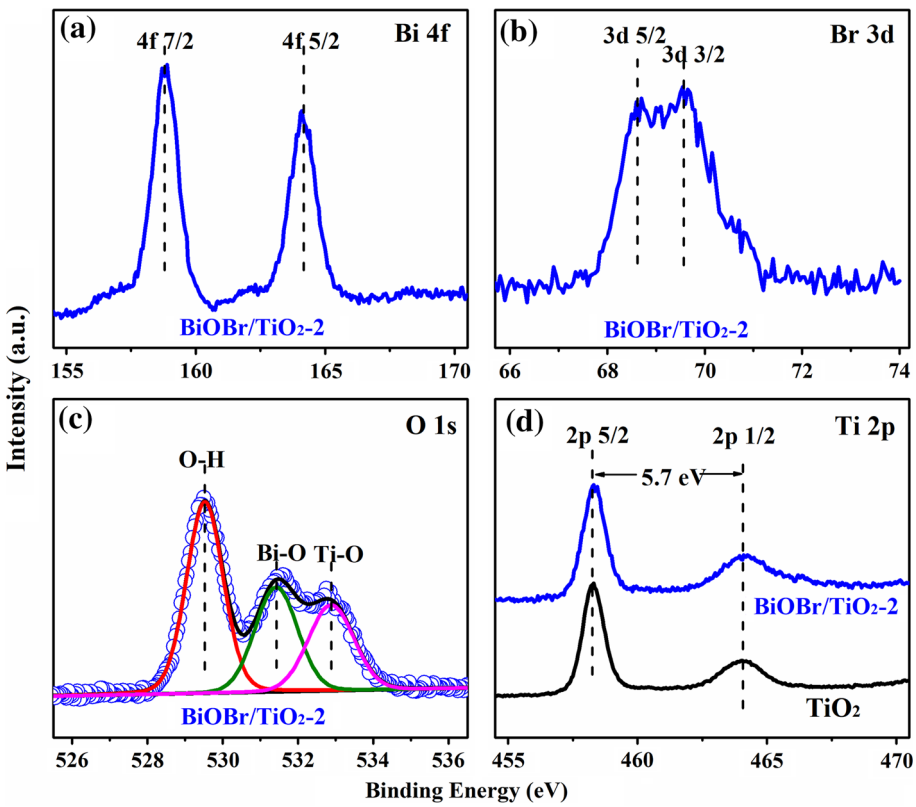


**Figure 3** XPS spectrum of **a** Bi 4f; **b** Br 3d; **c** O 1 s for BiOBr/$TiO_2$-2 and **d** Ti 2p for $TiO_2$ NFs and BiOBr/$TiO_2$-2.

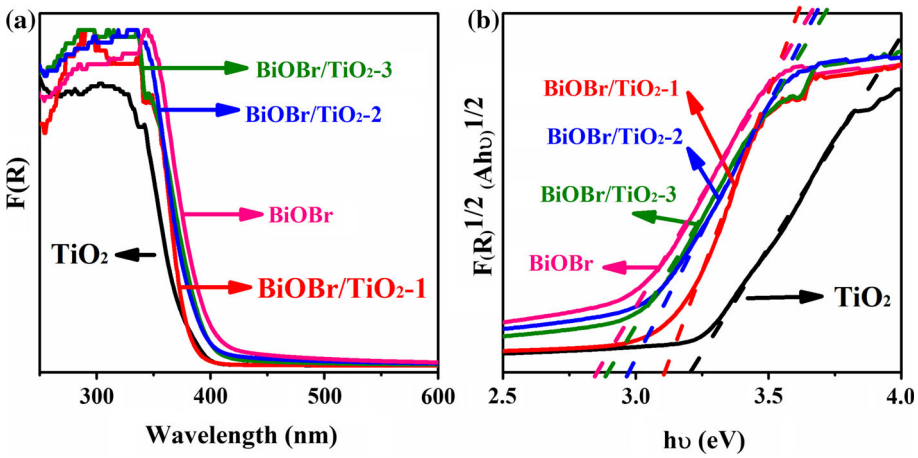


**Figure 4** **a** UV–Vis diffuses reflectance (DR) spectra and **b** the plots of $F(R)^{1/2}(Ahv)^{1/2}$ versus photon energy ($hv$) for $TiO_2$ NFs, BiOBr nanosheets and p-BiOBr/n-$TiO_2$ NFs.

$$R = R_{\text{Sample}}/R_{\text{BaSO}_4} \quad (2)$$

where $R$, $\alpha$ and $S$ are the reflectance, absorption coefficient and scattering coefficient, respectively. It can be seen that the absorption edge of the pure electrospun $TiO_2$ NFs and the absorption edge BiOBr nanosheets are located at about 393 and 355 nm, respectively. And the absorption edges of $p$-BiOBr/$n$-$TiO_2$ NFs show gradually a red-shift from 393 to 355 nm with the increased amount of BiOBr in the composite nanofibers. The band-gap energy of the $TiO_2$ and BiOBr was calculated by Eq. 3:

$$\alpha hv = A(hv - E_g)^{n/2} \quad (3)$$

where $\alpha$, $v$, $E_g$ and $A$ are the absorption coefficient, light frequency, band gap and a constant, respectively. Moreover, $n$ depends on the characteristics of the transition in a semiconductor: direct transition ($n = 1$) or indirect transition ($n = 4$). For $TiO_2$ and BiOBr, the value of $n$ is 4 for the indirect transition. Therefore, the band-gap energy of the $TiO_2$ and BiOBr in our experiment can be estimated from a plot of $(\alpha hv)^{1/2}$ versus photon energy $hv$. As observed in Fig. 4b, the band gap of $TiO_2$ and BiOBr is evaluated to be 3.2 eV and 2.8 eV, respectively, which is coincident with previous reports [44, 45]. Meanwhile, the band-gap energies of $p$-BiOBr/$n$-$TiO_2$ NFs are between that of $TiO_2$ and BiOBr and decreased with an increase in BiOBr's content in $p$-BiOBr/$n$-$TiO_2$ NFs.

The photocatalytic activity of the samples was evaluated by RhB and MO dyes. Figure 5a depicts the correlation curves between the concentration changes of dye molecules and the irradiation durations in the presence of photocatalysts. After UV-light irradiation for 20 min, the degradation efficiency of RhB is about 30, 57, 64, 89 and 76% for the electrospun $TiO_2$ NFs, mechanical mixture $TiO_2$ and BiOBr (M-BT, Bi:Ti = 1:0.20), BiOBr/$TiO_2$-1, BiOBr/$TiO_2$-2 and BiOBr/$TiO_2$-3, respectively. For a better comparison of the photocatalytic efficiency, the kinetic analysis of degradation of RhB is presented and discussed. In Fig. 5b, the kinetic linear simulation curves of the photocatalytic degradation of RhB of the $p$-BiOBr/$n$-$TiO_2$ NFs show that the above degradation reactions follow a Langmuir–Hinshelwood apparent first-order kinetics model. Due to the low initial concentrations of the reactants ($C_0$ = 10 mg/L in the present experiment), it could be simplified as the following equation [46]:

$$\ln C_0/C = kKt = k_{\text{app}}t \quad (4)$$

where $C$ is the concentration (mg/L), $t$ is the UV-light irradiation time, $k$ is the reaction rate constant (mg/(L min)), $K$ is the adsorption coefficient of the reactant (L/mg) and $k_{\text{app}}$ is the apparent first-order rate constant ($\text{min}^{-1}$). The order of photocatalytic activity is BiOBr/$TiO_2$-2 > BiOBr/$TiO_2$-3 > BiOBr/$TiO_2$-1 > M-BT > $TiO_2$, which is consistent with the activity studies above. The broad spectrum photocatalytic abilities of $p$-BiOBr/$n$-$TiO_2$ NFs have been further investigated by degradation of MO as pollutants in Fig. 5c. The highest photocatalytic degradation efficiency is also observed by BiOBr/$TiO_2$-2 as compared with the other samples. The kinetic linear simulation curves of the photocatalytic degradation of MO are shown in Fig. 5d. And the determined $k_{\text{app}}$ for different catalysts is also summarized in Table 1. Furthermore, the visible-light-driven photocatalytic degradation process ($\lambda > 400$ nm) was further carried out, and the

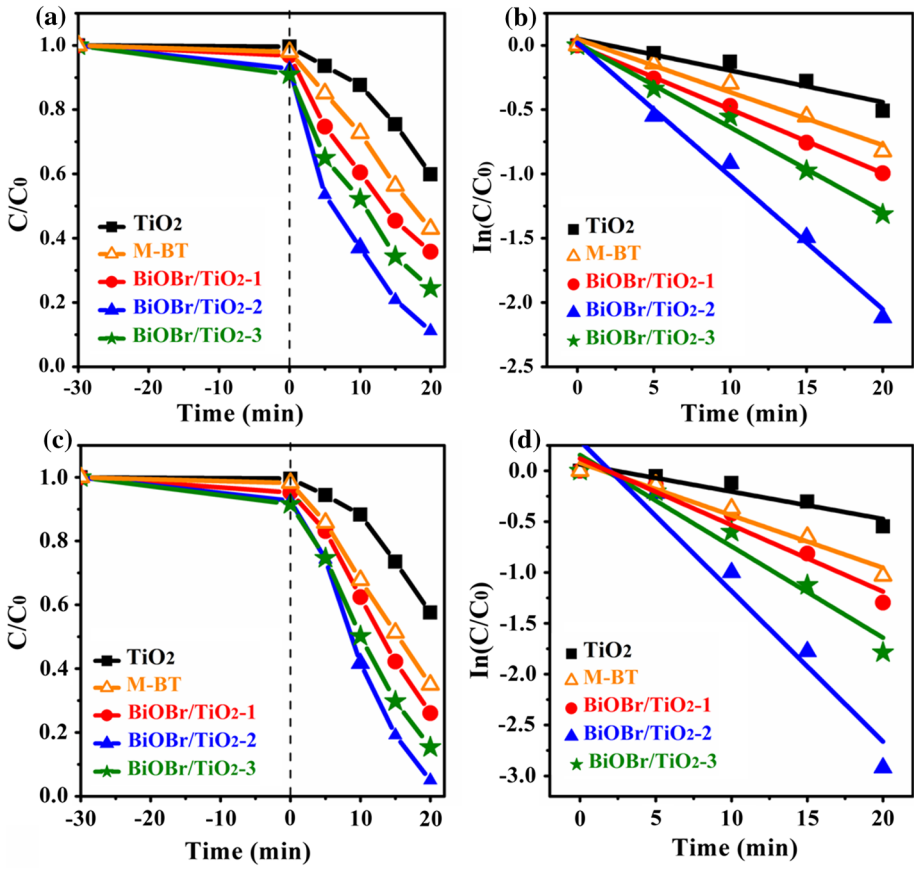


**Figure 5** Photocatalytic degradation and kinetic linear simulation curves of **a, b** RhB and **c**, **d** MO over $TiO_2$ NFs, *p*-BiOBr/*n*-$TiO_2$ NFs and M-BT under UV-light irradiation.

**Table 1** Amount of reactants, chemical component and photocatalysis reaction rates for $TiO_2$ NFs, *p*-BiOBr/*n*-$TiO_2$ NFs and M-BT

| Samples | Precursors (mM) | | Ti/Bi (molar ratio) | $K_{app}$ ($min^{-1}$) | |
|---|---|---|---|---|---|
| | $Bi(NO_3)_3$ | KBr | (EDX) | RhB | MO |
| $TiO_2$ | 0 | 0 | – | 0.034 ± 0.004 | 0.026 ± 0.005 |
| BiOBr/$TiO_2$-1 | 0.25 | 0.25 | 1:0.08 | 0.050 ± 0.001 | 0.065 ± 0.008 |
| BiOBr/$TiO_2$-2 | 0.5 | 0.5 | 1:0.20 | 0.103 ± 0.005 | 0.148 ± 0.018 |
| BiOBr/$TiO_2$-3 | 1 | 1 | 1:0.42 | 0.065 ± 0.003 | 0.089 ± 0.010 |
| M-BT | – | – | – | 0.047 ± 0.003 | 0.051 ± 0.005 |

corresponding results are shown in Figure S1. Among these samples, the BiOBr/$TiO_2$-2 also presents the optimal photocatalytic activity even though the existence of dye self-sensitized process upon visible-light excitation [47]. It further confirms the promoted charge separation at the hetero-interface of *p*-BiOBr/*n*-$TiO_2$ NFs.

It should be noted that the photocatalytic activities of *p*-BiOBr/*n*-$TiO_2$ NFs photocatalysts gradually increase with an increase in loaded-BiOBr content and reach the maximum value for the BiOBr/$TiO_2$-2 sample. After that, the activity of BiOBr/$TiO_2$-3 sequentially decreases. Obviously, the photocatalytic activity of the samples is significantly affected by the BiOBr content in *p*-BiOBr/*n*-$TiO_2$ NFs. According to the SEM images of *p*-BiOBr/*n*-$TiO_2$ NFs (Fig. 1), for low BiOBr content in the BiOBr/$TiO_2$-1 sample, sparse BiOBr nanosheets grown on $TiO_2$ NFs are observed. Thus, only a small number of *p*–*n* junctions are generated, leading to low photocatalytic activity. When the BiOBr content is increased in the BiOBr/$TiO_2$-2 sample, a large number of *p*–*n* junctions are formed. More *p*–*n* junctions can provide more separate paths for electrons and holes, resulting in the highest photocatalytic activity for the optimal BiOBr/$TiO_2$-2 sample. With further increase in BiOBr

content, dense BiOBr nanosheets cover the electrospun $TiO_2$ NFs, as observed in the BiOBr/$TiO_2$-3 sample (Fig. 1d), excess BiOBr will greatly increase thickness of shell structure which decreases the light irradiation on electrospun $TiO_2$ NFs and the *p*–*n* junction interfaces, leading to that the photoinduced electrons and holes have to experience a long diffusion length (Fig. 6a). As thus, the collision probability of the photoinduced carriers obviously increases before it reaches the interface. Most of them generate nonradiative recombination to release a number of phonons. This shielding effect of the dense BiOBr nanosheets coating the electrospun $TiO_2$ NFs makes the photocatalytic activity of the BiOBr/$TiO_2$-3 sample to decrease.

In addition, the photocatalytic degradation mechanism of dye pollutants by the *p*-BiOBr/*n*-$TiO_2$ NFs is systematically investigated by introducing ammonium oxalate (AO), Tert-butylalcohol (TBA), Cr(VI) and benzoquinone (BQ), which are known as effective holes ($h^+$), hydroxyl radicals (OH•), active electron ($e^-$) and superoxide radicals ($\bullet O_2$) scavengers for photocatalytic reaction, respectively (Fig. 6c). All scavengers are observed to partially suppress the photodegradation rates as compared to the absence of scavengers. The photodegradation rates decrease in the order of Cr(VI) < BQ < AO < TBA, indicating that $e^-$ and $\bullet O_2$ are the major reactive species in the photocatalytic process.

Based on the above results, a reasonable photocatalytic mechanism is proposed. For the *p*-type BiOBr, the Fermi energy level is close to the valence band, whereas for the *n*-type $TiO_2$, the Fermi energy level is close to the conduction band. When the two semiconductors are in contact to form a *p*–*n* junction (Fig. 6b), there is diffusion of electrons from $TiO_2$ to BiOBr due to their different Fermi energy levels, resulting in accumulation of negative charges in BiOBr close to the *p*–*n* heterojunction. At the same time, the holes transfer from BiOBr to $TiO_2$, leaving a positive section in $TiO_2$ near the *p*–*n* heterojunction. Moreover, the energy bands of BiOBr shift upward

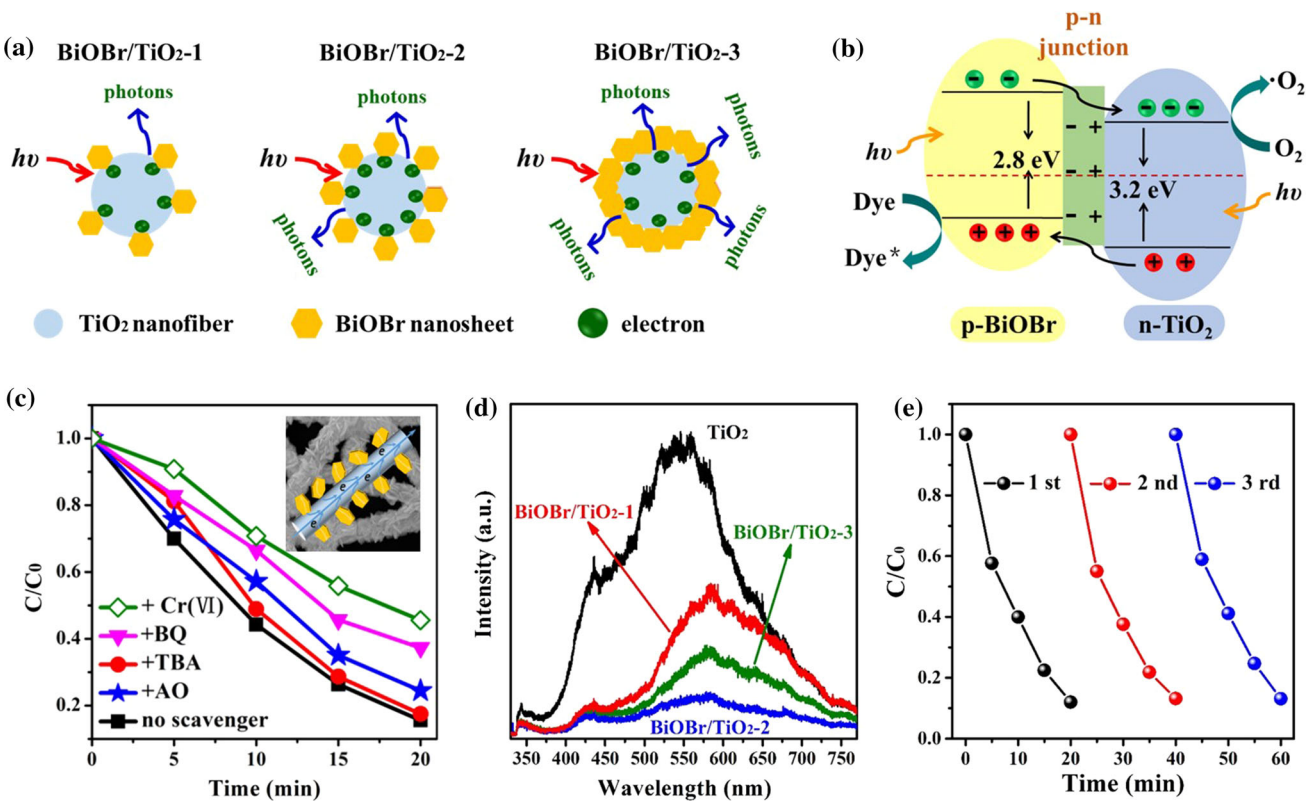


**Figure 6** **a** Schematic diagram on the influence of the content of BiOBr nanosheets; **b** possible photocatalytic reactions of *p*-BiOBr/*n*-$TiO_2$ NFs; **c** plots of photodegradation of RhB over BiOBr/$TiO_2$-2 with different scavengers and the inset is the SEM image and the schematic diagram of electron transfer for BiOBr/$TiO_2$-2; **d** PL emission spectra of $TiO_2$ NFs and *p*-BiOBr/*n*-$TiO_2$ NFs; **e** photocatalysis tests of BiOBr/$TiO_2$-2 for three cycles.

along the Fermi level and those of the $TiO_2$ shift downward along its Fermi level. With equilibration of BiOBr and $TiO_2$ Fermi levels, the diffusion of electrons from $TiO_2$ to BiOBr stops. Therefore, an equilibrium state is formed and an inner electric field will also be generated at the interface. Under UV-light irradiation, both BiOBr and $TiO_2$ are excited, and photoelectrons and holes are generated. The excited electrons on the conduction band of the *p*-type BiOBr transfer to that of *n*-type $TiO_2$, whereas the holes on the valence band of *n*-type $TiO_2$ transfer to that of the *p*-type BiOBr. Furthermore, the migration rates of the photoinduced electrons and holes are promoted by the internal electric field in the *p*-BiOBr/*n*-$TiO_2$ NFs, and the photocatalytic activity is largely enhanced.

The better separation of electrons and holes for *p*-BiOBr/*n*-$TiO_2$ NFs is also confirmed by photoluminescence spectrum (PL) in Fig. 6d, which can be used to investigate the relative quantum yields and trapping as well as transition of photoinduced electron–hole pairs. The higher PL intensity might indicate a higher recombination rate of photo-generated electrons and holes. Compared with electrospun $TiO_2$ NFs, the emission intensity from *p*-BiOBr/*n*-$TiO_2$ NFs is clearly reduced. This suggests that the recombination of photoinduced charge carriers can be effectively inhibited. Among the composite samples, BiOBr/$TiO_2$-2 shows the lowest intensity. Therefore, the unique heterostructured photocatalyst of *p*-BiOBr/*n*-$TiO_2$ NFs is highly favorable for efficiently separating the photoinduced carriers during the photocatalytic reactions.

To confirm the stability of the high photocatalytic performance of the BiOBr/$TiO_2$-2 photocatalysts, the circulating runs in the photodegradation of RhB were checked. Each experiment is carried out under identical conditions. As shown in Fig. 6e, the photocatalytic activity of the BiOBr/$TiO_2$-2 remained almost unchanged after three cycles clearly indicating the stability.

## Conclusions

In summary, *p*-BiOBr/*n*-$TiO_2$ NFs photocatalysts have been prepared through combining electrospinning technique with solvothermal method. The morphologies of secondary BiOBr nanostructures can be facilely tuned by adjusting the amount of Bi source and Br source during the solvothermal process. The obtained *p*-BiOBr/*n*-$TiO_2$ NFs exhibited higher photocatalytic activity than pure electrospun $TiO_2$ NFs and M-BT for the degradation of RhB and MO under UV-light irradiation. This enhanced photocatalytic activity is ascribed to the following synergistic effects: (a) formation of the *p*–*n* junction, which enhances the separation of photoinduced carriers; (b) 1D nanofiber heterostructure, which is favorable for high efficiency and directional transport and separation of electrons and holes. Moreover, the 3D nanostructure for *p*-BiOBr/*n*-$TiO_2$ NFs is beneficial to separate from liquid solution for recycling utilization avoiding secondary pollution. Therefore, this work provides a general and effective method for fabricating *p*-BiOBr/*n*-$TiO_2$ NFs photocatalyst. Moreover, this route can offer new insight into the design and fabrication of other advanced materials with heterojunction structures for photocatalytic applications.

## Acknowledgements

This work was supported by the National Natural Science Foundation of China under (Grant Nos. 51772041, 60876014, 51302128), the Natural Science Foundation of Henan Province (Grant Nos. 19A430020, 132300410085, 142300410024, 172102210398, 18B140007), the Program for Youth Scholar Teachers Supporting Plan in Universities of Henan Province (2015GGJS-112), the Natural Science Foundation of Liaoning Province (Grant No. 20170540190), the Program for Liaoning Excellent Talents in University (LNET) (Grant No. LR2017004) and the Program for Dalian Excellent Talents (Grant No. 2016RQ069).

## Compliance with ethical standards

**Conflict of interest** The authors declare that there is no conflict of interest regarding the publication of this paper.

**Electronic supplementary material:** The online version of this article (https://doi.org/10.1007/s10853-019-03466-z) contains supplementary material, which is available to authorized users.

## References


[1] Hiroshi Y, Yukiyasu Y, Hideo T (1979) Heterogeneous photocatalytic reduction of dichromate on *n*-type semiconductor catalysts. Nature 282:817–818

[2] Zhang Z, Liu Y, Fang Y, Cao B, Huang J, Liu K, Dong B (2018) Near-infrared-plasmonic energy upconversion in a nonmetallic heterostructure for efficient $H_2$ evolution from ammonia borane. Adv Sci 5(9):1800748-1–1800748-9

[3] Yang MQ, Zhang N, Pagliaro M, Xu YJ (2014) Artificial photosynthesis over graphene-semiconductor composites. Are we getting better? Chem Soc Rev 43(24):8240–8254

[4] Zhou Y, Zhang S, Ding Y, Zhang L, Zhang C, Zhang X, Zhao Y, Yu G (2018) Efficient solar energy harvesting and storage through a robust photocatalyst driving reversible redox reactions. Adv Mater 30(31):1802294-1–1802294-7

[5] Wu J, Zhang Z, Liu B, Fang Y, Wang L, Dong B (2018) UV–Vis-NIR-driven plasmonic photocatalysts with dual-resonance modes for synergistically enhancing $H_2$ generation. Solar RRL 2(6):1800039-1–1800039-8

[6] Zhang Z, Huang J, Fang Y, Zhang M, Liu K, Dong B (2017) A nonmetal plasmonic Z-scheme photocatalyst with UV-to NIR-driven photocatalytic protons reduction. Adv Mater 29(18):1606688-1–1606688-9

[7] Wang H, Sun X, Li D, Zhang X, Chen S, Shao W, Tian Y, Xie Y (2017) Boosting hot-electron generation: exciton dissociation at the order-disorder interfaces in polymeric photocatalysts. J Am Chem Soc 139:2468–2473

[8] Linsebigler AL, Lu G, Yates JT (1995) Photocatalysis on $TiO_2$ surfaces: principles, mechanisms, and selected results. Chem Rev 95(3):735–758

[9] Zhang Z, Dong B, Zhang M, Huang J, Lin F, Shao C (2014) Electrospun Pt/$TiO_2$ hybrid nanofibers for visible-light-driven $H_2$ evolution. Int J Hydrog Energy 39(34):19434–19443

[10] Wu K, Dong X, Zhu J et al (2018) Designing biomimetic porous celery: $TiO_2$/ZnO nanocomposite for enhanced $CO_2$ photoreduction. J Mater Sci 53:11595–11606. https://doi.org/10.1007/s10853-018-2397-y

[11] Meng A, Zhang L, Cheng B, Yu J (2018) $TiO_2$–MnOx–Pt hybrid multiheterojunction film photocatalyst with enhanced photocatalytic $CO_2$-reduction activity. ACS Appl Mater Interfaces. https://doi.org/10.1021/acsami.8b02552

[12] Zhang Z, Jiang X, Liu B, Guo L, Lu N, Wang L, Huang J, Liu K, Dong B (2018) IR-driven ultrafast transfer of plasmonic hot electrons in nonmetallic branched heterostructures for enhanced $H_2$ generation. Adv Mater 30(9):1705221-1–1705221-10

[13] Wang Y, Wu QH, Li Y et al (2018) Controlled fabrication of $TiO_2$/$C_3N_4$ core–shell nanowire arrays: a visible-light-responsive and environmental-friendly electrode for photoelectrocatalytic degradation of bisphenol A. J Mater Sci 53:11015–11026. https://doi.org/10.1007/s10853-018-2368-3

[14] Wang ZH, Luo CZ, Zhang YP et al (2018) Construction of hierarchical $TiO_2$ nanorod array/graphene/ZnO nanocomposites for high-performance photocatalysis. J Mater Sci 53:15376–15389. https://doi.org/10.1007/s10853-018-2724-3

[15] Liu HJ, Thind SS, Wu GS, Wen JL, Chen AC (2015) Synthesis and photoelectrochemical studies of N, Zr co-doped mesoporous titanium dioxide. J Electroanal Chem 736:93–100

[16] Wang YZ, Zu M, Li S, Butburee T, Wang LZ, Peng F, Zhang SQ (2017) Dual modification of $TiO_2$ nanorods for selective photoelectrochemical detection of organic compounds. Sens Actuator B Chem 250:307–314

[17] Wang K, Shao C, Li X, Zhang X, Lu N, Miao F, Liu Y (2015) Hierarchical heterostructures of *p*-type BiOCl nanosheets on electrospun *n*-type $TiO_2$ nanofibers with enhanced photocatalytic activity. Catal Commun 67:6–10

[18] Song XC, Li WT, Huang WZ, Zhou H, Zheng YF, Yin HY (2015) A novel *p–n* heterojunction BiOBr/$ZnWO_4$: preparation and its improved visible light photocatalytic activity. Mater Chem Phys 160:251–256

[19] Ji L, Wang HR, Yu RM (2014) Preparation, characterization and visible-light photocatalytic activities of *p–n* heterojunction BiOBr/$NaBiO_3$ composites. Chem J Chin 35(10):2170–2176

[20] Wang S, Wang L, Ma W, Johnson DM, Fang Y, Jia M, Huang Y (2015) Moderate valence band of bismuth oxyhalides (BiOXs, X = Cl, Br, I) for the best photocatalytic degradation efficiency of MC-LR. Chem Eng J 259:410–416

[21] Zhang X, Li B, Wang J, Yuan Y, Zhang Q, Gao Z, Liu L-M, Chen L (2014) The stabilities and electronic structures of single-layer bismuth oxyhalides for photocatalytic water splitting. Phys Chem Chem Phys 16(47):25854–25861

[22] Cheng H, Huang B, Dai Y (2014) Engineering BiOX (X = Cl, Br, I) nanostructures for highly efficient photocatalytic applications. Nanoscale 6(4):2009–2026

[23] Wang H, Chen S, Yong D, Zhang X, Li S, Shao W, Sun X, Pan B, Xie Y (2017) Giant electron–hole interactions in confined layered structures for molecular oxygen activation. J Am Chem Soc 139:4737–4742

[24] Wang H, Yong D, Chen S, Jiang S, Zhang X, Shao W, Zhang Q, Yan W, Pan B, Xie Y (2018) Oxygen-vacancy-mediated exciton dissociation in BiOBr for boosting charge-carrier-involved molecular oxygen activation. J Am Chem Soc 140:1760–1766

[25] Liu C, Xu Q, Zhang Q et al (2019) Layered BiOBr/$Ti_3C_2$ MXene composite with improved visible-light photocatalytic

activity. J Mater Sci 54:2458–2471. https://doi.org/10.1007/s10853-018-2990-0

[26] Huo Y, Zhang J, Miao M, Jin Y (2012) Solvothermal synthesis of flower-like BiOBr microspheres with highly visible-light photocatalytic performances. Appl Catal B 111–112:334–341

[27] Fan Z, Zhao Y, Zhai W, Qiu L, Li H, Hoffmann MR (2016) Facet-dependent performance of BiOBr for photocatalytic reduction of Cr(VI). RSC Adv 6(3):2028–2031

[28] Li H, Hu T, Liu J, Song S, Du N, Zhang R, Hou W (2016) Thickness-dependent photocatalytic activity of bismuth oxybromide nanosheets with highly exposed (010) facets. Appl Catal B 182:431–438

[29] Peng Y, Xu J, Liu T, Y-g M (2017) Controlled synthesis of one-dimensional BiOBr with exposed (110) facets and enhanced photocatalytic activity. CrystEngComm 19(43):6473–6480

[30] Ye L, Su Y, Jin X, Xie H, Zhang C (2014) Recent advances in BiOX (X = Cl, Br and I) photocatalysts: synthesis, modification, facet effects and mechanisms. Environ Sci Nano 1(2):90–112

[31] Cai L, Zhang G, Zhang Y, Wei Y (2018) Mediation of band structure for $BiOBr_xI_{1-x}$ hierarchical microspheres of multiple defects with enhanced visible-light photocatalytic activity. CrystEngComm 20(26):3647–3656

[32] Liu H, Du C, Li M, Zhang S, Bai H, Yang L, Zhang S (2018) One-pot hydrothermal synthesis of $SnO_2$/BiOBr heterojunction photocatalysts for the efficient degradation of organic pollutants under visible light. ACS Appl Mater Interfaces 10:28686–28694

[33] Wang XJ, Yang WY, Li FT, Zhao J, Liu RH, Liu SJ, Li B (2015) Construction of amorphous $TiO_2$/BiOBr heterojunctions via facets coupling for enhanced photocatalytic activity. J Hazard Mater 292:126–136

[34] Wei XX, Cui H, Guo S, Zhao L, Li W (2013) Hybrid BiOBr–$TiO_2$ nanocomposites with high visible light photocatalytic activity for water treatment. J Hazard Mater 263:650–658

[35] Zhang J, Zhang L, Lv J, Zhou S, Chen H, Zhao Y, Wang X (2014) Exceptional visible-light-induced photocatalytic activity of attapulgite–BiOBr–$TiO_2$ nanocomposites. Appl Clay Sci 90:135–140

[36] Lu N, Zhang Z, Wang Y, Liu B, Guo L, Wang L, Huang J, Liu K, Dong B (2018) Direct evidence of IR-driven hot electron transfer in metal-free plasmonic $W_{18}O_{49}$/carbon heterostructures for enhanced catalytic $H_2$ production. Appl Catal B 233:19–25

[37] Song L, Jing W, Chen J et al (2019) High reusability and durability of carbon-doped $TiO_2$/carbon nanofibrous film as visible-light-driven photocatalyst. J Mater Sci 54:3795–3804. https://doi.org/10.1007/s10853-018-3105-7

[38] Liu Y, Zhang M, Li L, Zhang X (2014) One-dimensional visible-light-driven bifunctional photocatalysts based on $Bi_4Ti_3O_{12}$ nanofiber frameworks and $Bi_2XO_6$ (X = Mo, W) nanosheets. Appl Catal B 160–161:757–766

[39] Zhang Z, Huang Y, Liu K, Guo L, Yuan Q, Dong B (2015) Multichannel-improved charge-carrier dynamics in well-designed hetero-nanostructural plasmonic photocatalysts toward highly efficient solar-to-fuels conversion. Adv Mater 27(39):5906–5914

[40] Di J, Xia J, Ji M, Wang B, Yin S, Zhang Q, Chen Z, Li H (2016) Advanced photocatalytic performance of graphene-like BN modified BiOBr flower-like materials for the removal of pollutants and mechanism insight. Appl Catal B 183:254–262

[41] Ye L, Jin X, Liu C, Ding C, Xie H, Chu KH, Wong PK (2016) Thickness-ultrathin and bismuth-rich strategies for BiOBr to enhance photoreduction of $CO_2$ into solar fuels. Appl Catal B 187:281–290

[42] Yu JC, Zhang L, Zheng Z, Zhao J (2003) Synthesis and characterization of phosphated mesoporous titanium dioxide with high photocatalytic activity. Chem Mater 15(11):2280–2286

[43] Pian X, Lin B, Chen Y, Kuang J, Zhang K, Fu L (2011) Pillared nanocomposite $TiO_2$/Bi-doped hexaniobate with visible-light photocatalytic activity. J Phys Chem C 115(14):6531–6539

[44] Wang K, Shao C, Li X, Miao F, Lu N, Liu Y (2016) Heterojunctions of *p*-BiOI nanosheets/*n*-$TiO_2$ nanofibers: preparation and enhanced visible-light photocatalytic activity. Materials 9(2):90-1–90-12

[45] Cui Y, Jia Q, Li H, Han J, Zhu L, Li S, Zou Y, Yang J (2014) Photocatalytic activities of $Bi_2S_3$/BiOBr nanocomposites synthesized by a facile hydrothermal process. Appl Surf Sci 290:233–239

[46] Lee MS, Park SS, Lee G, Ju C, Hong S (2005) Synthesis of $TiO_2$ particles by reverse microemulsion method using nonionic surfactants with different hydrophilic and hydrophobic group and their photocatalytic activity. Catal Today 101(3–4):283–290

[47] Zhang ZY, Shao CL, Li XH, Sun YY, Zhang MY, Mu JB, Zhang P, Guo ZC, Liu YC (2013) Hierarchical assembly of ultrathin hexagonal $SnS_2$ nanosheets onto electrospun $TiO_2$ nanofibers: enhanced photocatalytic activity based on photoinduced interfacial charge transfer. Nanoscale 5:606–618